Available online at www.sciencedirect.com
ScienceDirect
Composites Science and Technology 67 (2007) 1694–1708
COMPOSITES SCIENCE AND TECHNOLOGY
www.elsevier.com/locate/compscitech

Multiscale modeling of solid propellants: From particle packing to failure

K. Matouš [a,c,*,1], H.M. Inglis [a,2], X. Gu [a,2], D. Rypl [b,3], T.L. Jackson [a,2], P.H. Geubelle [c,1]

[a] Center for Simulation of Advanced Rockets, University of Illinois at Urbana-Champaign, Urbana, IL 61801, USA
[b] Department of Structural Mechanics, Czech Technical University in Prague, Prague 160 00 P6, Czech Republic
[c] Department of Aerospace Engineering, University of Illinois at Urbana-Champaign, Urbana, IL 61801, USA

Received 17 January 2006; received in revised form 24 May 2006; accepted 29 June 2006
Available online 1 September 2006

Abstract

We present a theoretical and computational framework for modeling the multiscale constitutive behavior of highly filled elastomers, such as solid propellants and other energetic materials. Special emphasis is placed on the effect of the particle debonding or dewetting process taking place at the microscale and on the macroscopic constitutive response. The microscale is characterized by a periodic unit cell, which contains a set of hard particles (such as ammonium perchlorate for AP-based propellants) dispersed in an elastomeric binder. The unit cell is created using a packing algorithm that treats the particles as spheres or discs, enabling us to generate packs which match the size distribution and volume fraction of actual propellants. A novel technique is introduced to characterize the pack geometry in a way suitable for meshing, allowing for the creation of high-quality periodic meshes with refinement zones in the regions of interest. The proposed numerical multiscale framework, based on the mathematical theory of homogenization, is capable of predicting the complex, heterogeneous stress and strain fields associated, at the microscale, with the nucleation and propagation of damage along the particle–matrix interface, as well as the macroscopic response and mechanical properties of the damaged continuum. Examples involving simple unit cells are presented to illustrate the multiscale algorithm and demonstrate the complexity of the underlying physical processes.

Keywords: A. Particle-reinforced composites; B. Debonding; B. Microstructure; C. Damage mechanics; Mathematical homogenization

1. Introduction

Particulate elastomeric matrix composites are used today in a variety of applications such as solid rocket propellants, energetic materials and automobile tires. The very complex mechanical behavior of these materials is driven by the complicated microstructure and physical processes occurring in the body at multiple length scales under mechanical loading. A key source of such processes appears to be associated with microcracks initiating and growing along the matrix–particle interface and with the nucleation and coalescence of voids in the matrix.

How to model these complex materials and damage processes has been a long standing quest. Ha et al. [1] and Simo [2] studied viscoelasticity with growing damage; Mullins [3] discovered the Mullins effect, Farris [4] studied vacuole formation and growth and Christensen et al. [5] proposed models for stiffness reduction in coated particles and/or fibers. Interface friction or sliding theories have also been investigated by Hutchinson et al. [6]; Hashin [7]

* Corresponding author. Address: Center for Simulation of Advanced Rockets, University of Illinois at Urbana-Champaign, Urbana, IL 61801, USA. Tel.: +1 217 333 8448; fax: +1 217 333 8497.
E-mail addresses: matous@uiuc.edu (K. Matouš), hinglis@uiuc.edu (H.M. Inglis), xgu1@uiuc.edu (X. Gu), drypl@fsv.cvut.cz (D. Rypl), tlj@csar.uiuc.edu (T.L. Jackson), geubelle@uiuc.edu (P.H. Geubelle).
[1] Supported by the US Department of Energy under contract number
[2] Supported by the US Department of Energy under contract number B341494.
[3] Supported by the Grant Agency of the Czech Republic under contract number GACR 103/05/2315.

0266-3538/$ - see front matter © 2006 Elsevier Ltd. All rights reserved.
doi:10.1016/j.compscitech.2006.06.017

provided analytical expressions of local and overall stress and strain fields as functions of the phase moduli and interfacial properties. Another group of models published in recent years devoted to progressive interfacial decohesion and/or progressive volumetric damage has been proposed by Matouš [8], Krajcinovic [9] and Chaboche et al. [10]. Zhong and Knauss employed a cohesive model to resolve the debonding of rigid particles from an elastomeric matrix [11,12]. Also, three-dimensional periodic cells were recently used by Michel et al. [13] and Llorca and Segurado [14,15] in their study of elastic and elasto-plastic particulate composites. In their work, Llorca and Segurado considered simple periodic boundary conditions without interfacial damage and no mathematical theory of homogenization (MTH) was employed. Moreover, difficulties with mesh generation were discussed. Three faces of a cube were meshed with quadratic triangles, and the meshes were manually copied to the opposite sides. Such an approach is bypassed here and novel meshing of periodic structures is proposed as part of an automated numerical framework to model particulate composites from packing to failure. Note that the emphasis of this paper is not to investigate the size of the representative volume element. Instead, we investigate hereafter the damage response of a periodic unit cell (PUC).

The mathematical/numerical framework described in this paper consists of several fully automated components. First, a packing algorithm developed in [16,17] is used to create the characteristic pack matching the particle distribution and volume fraction. Next, a pre-processing procedure is applied to create a geometric model with refinement zones in the regions of interest. Once the pre-processing is performed and the geometric model is created, we employ the $T3d$ mesh generator developed by Rypl [18,19] to discretize a periodic unit cell. $T3d$ is based on an advancing front technique and can mesh complex two-dimensional (2D) and three-dimensional (3D) domains into triangular and tetrahedral meshes of a high quality. Moreover, mixed meshes consisting of quadrilaterals and triangles are allowed for 2D domains. This feature is of great interest, since meshes composed of triangles are known to be subject to locking for nearly incompressible materials. In this work, with examples dedicated primarily to the 2D case, the $\overline{\boldsymbol{B}}$ (Bbar) procedure [20] is used to eliminate the pressure instabilities associated with material incompressibility. In particular, $Q1/P0$ elements, where the displacement field is approximated by a bilinear function and the pressure is constant over the element, are used and despite the fact that this element violates the Babuška-Brezzi stability conditions, an optimal convergence rate can be proven under suitable assumptions (see [20] for more details). A novel stabilized finite element framework was used for 3D finite strain analysis by Matouš and Geubelle [21]. The mechanical behavior of the interface between particles and a blend (composed of the elastomeric matrix and the particles too small to be incorporated in the unit cell) is modeled by a cohesive law, which is embedded in the finite element implementation of the mathematical theory of homogenization.

The mathematical theory of homogenization, including the cohesive model, is described in Section 3. This theory is very popular in computational multiscale modeling and has been used by several researchers [22,23]. The finite strain counterpart of this theory was described in [21]. Next, various 2D examples involving the multiaxial loading of an idealized propellant are presented, showing the ability of the proposed multiscale scheme to relate the damage processes taking place at the microscale to the macroscopic constitutive relations. As illustrated in these examples, one of the key aspects of the proposed scheme is its ability to capture the complex interactions between the closely packed particles.

The symbolic notation adopted herein uses upper case boldface italic and lower case boldface Greek letters, e.g., $\boldsymbol{P}$ and $\boldsymbol{\sigma}$ for second-order tensors. The trace of the second-order tensor is denoted as $\mathrm{tr}(\boldsymbol{A})$, and the tensor operations between two second-order tensors $\boldsymbol{S}$ and $\boldsymbol{E}$ are indicated as $\boldsymbol{SE}$ for a contraction of tensors (a second-order tensor) or $\boldsymbol{S}:\boldsymbol{E}$ for the scalar product (a double contraction). A quantity marked by an underline, $\underline{\epsilon}$, denotes the quantity ϵ at the macroscale. Other notational conventions adopted in this paper are introduced as they are used.

2. Packing algorithm, pre-processing and meshing procedures

To achieve an accurate description of the damage evolution in heterogeneous materials, it is often essential to perform the microscale analysis on a representative volume element that adequately captures the heterogeneous microstructure. This computational description of the representative volume element is particularly challenging in the case of highly packed particulate composites, such as solid propellants, due to the geometrical constraints associated with the small inter-particle distances and with the range of particle sizes needed to achieve the high particle volume fraction. To that effect, we have developed a fully automated process that involves a dynamic packing algorithm used to create a computational description of the embedded particles, a pre-processing procedure to eliminate the singularities inherent in contacting particles, and a very general meshing tool to generate a high-quality periodic finite element discretization of the periodic unit cell. These three pre-processing tools are described next.

2.1. Rocpack – a dynamic packing algorithm

The heterogeneous propellants of interest consist of ammonium perchlorate oxidizer (AP) and aluminum (Al) particles embedded in a fuel polymeric binder. Typical loadings are 80–87% by weight AP if no aluminum is present; 68–76% by weight AP and 10–18% by weight Al

otherwise. It has long been recognized that various characteristics, such as the burning rate or the response to dynamic loading, of a heterogeneous propellant are influenced by the propellant morphology, by the size and size distribution of the AP particles. It follows that any serious attempt to describe the characteristics of heterogeneous propellants must include a packing algorithm, a strategy for defining and constructing a model propellant. Lattice (or crystal) packs are easily defined, but do not reflect the random nature of a true propellant. For this, a random packing algorithm must be used, and a suitable one, called *Rocpack*, is defined and discussed in [16,17]. This algorithm is dynamic in nature and can closely pack spheres or discs of arbitrary size. The algorithm has recently been extended to ellipsoids to study non-isotropic packs [24]. For completeness, we briefly describe the algorithm here.

The algorithm begins with an infinite computational domain defined by the periodic continuation of a cube, and points are randomly assigned to this domain at time $t = 0$ with random velocities. For $t > 0$, the points become spheres that grow linearly in time with a distribution of rates that defines the final distribution of AP and Al diameters. Collisions between the particles are dealt with using straightforward but non-classical dynamics, and this prevents overlapping. The pack is defined by stopping the calculation at some assigned volume fraction (defined as the total volume of the spheres to the volume of the cube), or after the interval between collisions becomes too small to continue. The output is a random distribution of spheres with centers $\boldsymbol{Y}_i$ and radii r_i, where subscript "i" represents the particle index.

We use the data of McGeary [25], who packed bimodal steel shot in a cylindrical container, to validate the packing code. Fig. 1 shows comparisons between the experimental data and the numerical data for two bimodal mixes. In each case the fine particles have a single diameter of 360 μm, and the ratio of coarse to fine particles is 3.44 (top panel) and 4.77 (bottom panel). In each panel the percent of fine particle is varied from zero (all coarse; monomodal) to 100 (all fine; monomodal). Note the excellent agreement between experimental data and numerical results. Also note that, for the 3.44 ratio case, we were able to generate slightly higher volume fractions than that obtained experimentally in the range of 10–30% fine mode. The slight over prediction in packing fraction is due to the difficulty in packing bimodal steel and comparison with experimental data is only informative. We do not have detailed information about experiments (number of tests, error bars, etc.)

Packs generated in this fashion can be designed to capture the volume fractions of various sized particles in experimental or industrial packs. Fig. 2 shows an example of a periodic pack generated with 10,000 particles per cube, colored according to particle diameter. The binder fills the space between particles. This pack mimics a propellant built and burnt by Miller [26].

From packs as described above, a periodic unit cell of much smaller size can be derived. As shown in [27], the periodic unit cell can possesses the same material statistics as the original characteristic pack. Hence, the computer grown pack obtained by particle packing is used as a digital representation of a microcontinuum.

2.2. Pre-processing procedure

Although the output from the packing algorithm described above is geometrically very simple, it is unsuitable to be used directly in a numerical framework as contacting particles would lead to singularities. Moreover, as indicated earlier, the proximity of adjacent, closely packed particles poses some important challenges in the

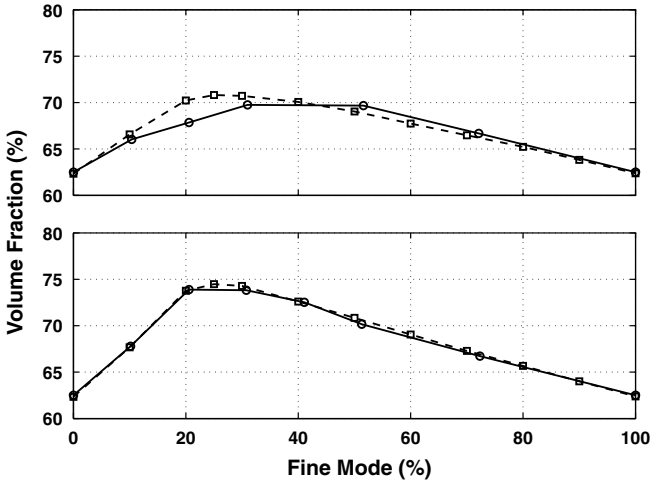

Fig. 1. Volume fraction for a coarse to fine ratio of 3.44 (top) and 4.77 (bottom) bimodal mix; numerical (dash; box) and experimental (solid; circle). The fine particles have a single diameter of 360 μm.

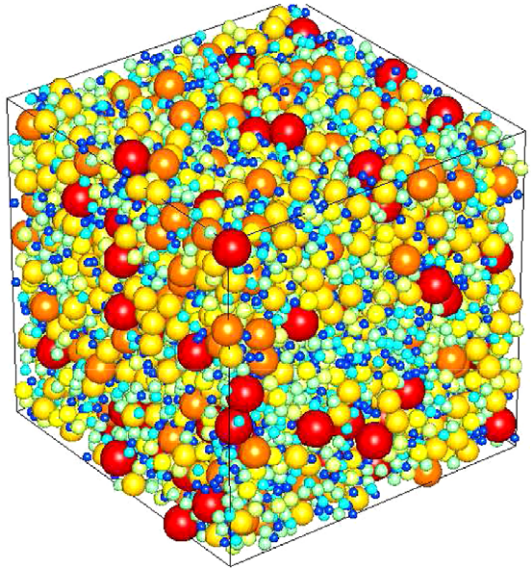

Fig. 2. A typical randomly generated propellant pack with 10,000 spheres, colored according to particle diameter.

finite element discretization of the periodic unit cell, because very small elements need to be used in some regions of the cell. A uniform finite element discretization would result in a prohibitively large number of degrees of freedom. Therefore, a more sophisticated approach needs to be adopted to mesh a unit cell. In the present work, the geometry is characterized by rational Bezier curves and/or surfaces, and the general meshing tool *T3d* developed by Rypl [18,19] is employed to discretize the microstructure as described below. This meshing framework can automatically provide non-uniform 2D–3D meshes with refinement zones in regions of interest, such as particles in close proximity, where the stress concentration will be pronounced and a fine mesh is required. It also allows for the generation of periodic meshes needed to enforce the periodicity of the microscopic solutions obtained as part of the mathematical theory of homogenization.

A pre-processing algorithm is developed to create the geometric model from the *Rocpack* output: shrink particles in contact with other particles and/or the reference box and compute the refinement parameters. The separation distance between particles i and j is computed simply as

$$\omega_{ij} = \|\boldsymbol{Y}_i - \boldsymbol{Y}_j\| - (r_i + r_j). \tag{1}$$

Whenever $\omega_{ij} < \alpha$, the radii of the corresponding particles i and j are modified according to

$$\begin{aligned} r_i^{\text{new}} &= r_i - (\alpha - \omega_{ij})\frac{r_i}{r_i + r_j}, \\ r_j^{\text{new}} &= r_j - (\alpha - \omega_{ij})\frac{r_j}{r_i + r_j}. \end{aligned} \tag{2}$$

Here, α represents a user-defined minimum separation between the surfaces of adjacent particles.

The volume change associated with particle shrinking is added to the blend, which consists of a binder and small particles not accounted for in the packing procedure. Then, the spatially-dependent refinement factor $\eta_{ij} \in (0,1)$, which modifies the user-prescribed element size h, is given by

$$\eta_{ij} = \begin{cases} 0.1 + \frac{0.9}{\beta - \alpha}(\omega_{ij} - \alpha) & \text{if } \alpha \leqslant \omega_{ij} \leqslant \beta, \\ 1.0 & \text{if } \omega_{ij} \geqslant \beta, \end{cases} \tag{3}$$

where β is the maximum distance influenced by refinement (second user-defined parameter). Thus, the geometric model and the resulting mesh depend on two parameters α and β, and the default mesh size h, respectively. All parameters α, β, h must be suitably chosen; therefore, the pre-processing and meshing procedures require some trial and error to determine the minimum and maximum particle radius, mesh density, etc.

2.3. Meshing tool – periodic mesh

One possible choice for prescribing the periodic boundary conditions required in the mathematical theory of homogenization is to assign the same deformation identification numbers to the corresponding degrees of freedom related to nodes on opposite sides of the unit cell. Thus, the periodic constraints are imposed directly on the discrete unknowns in the finite element solution procedure. We have thus modified *T3d* to discretize pairs of model surfaces on opposite sides of the PUC by topologically and geometrically identical meshes. However, this can only be successfully accomplished under certain conditions. First, the opposite surfaces must be geometrically identical. Second, they must be topologically identical, i.e., the ordering of curves bounding the surfaces and their orientation with respect to the surface normal must be exactly the same.[4] Both conditions are directly satisfied by the adopted pre-processing procedure.

The discretization engine *T3d* is based on the advancing front technique and can provide high-quality unstructured surface and solid meshes. Assuming that the opposite surfaces are topologically and geometrically identical, one may get the impression that exactly the same meshes must be produced if the advancing front on both surfaces is initialized identically. But this is true only if the same mesh density control is used and if precise arithmetics without round-off error is considered. However, neither of these two conditions are usually satisfied. Therefore, a different approach based on *mirroring* surface meshes on opposite sides of the PUC has been adopted. This approach requires that there is a parametric space associated with each of the mirrored surfaces (mirror master surface on one side and mirror slave surface on the opposite side of the PUC) and that the mapping between the parametric and real spaces is identical for both of them. This is again achieved by the pre-processing procedure that sets up the pairs of opposite mirrored surfaces.

The mirror master surface is discretized in the standard way using the advancing front technique [28]. On the mirror slave surface, nodes with the same parametric coordinates as their counterparts on the mirror master surface are created (Fig. 3). Their real coordinates are given by the mapping applied to the geometry of the mirror slave surface. Each of the nodes on the mirror master surface temporarily stores a pointer to its counterpart on the mirror slave surface. Similar pointers are also established on curves bounding the mirror master surface. The final mesh on the mirror slave surface is then generated by traversing the elements on the mirror master surface and creating for each of them a new element on the mirror slave surface using the nodes being stored as pointers at the nodes of the original element on the mirror master surface (Fig. 3). After all elements on a particular mirror slave surface are formed, the

[4] Note that *T3d* is based on a Bezier representation of curves and surfaces. Thus, a surface is defined by a list of clockwise or counterclockwise oriented boundary curves each of which is in turn topologically defined by a starting and an ending vertex.

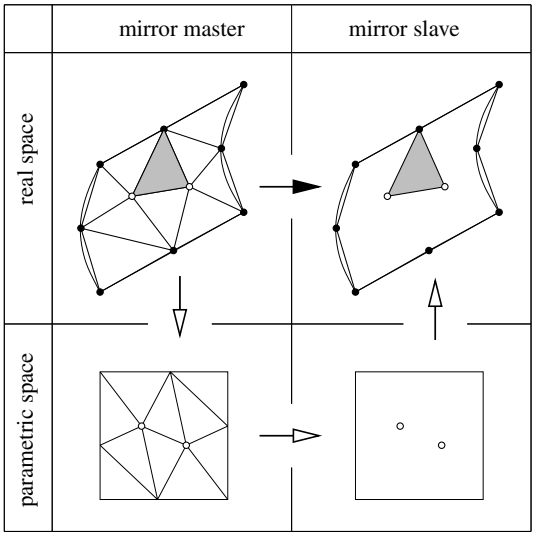

Fig. 3. Mirroring of surface mesh. The arrows visualize the flow of information to create nodes (empty arrows) and to form elements (full arrows) on the mirror slave surface.

pointers to slave nodes on the mirror master surface and its boundary curves are discarded. In this way, topologically identical meshes of the same geometry are produced for all pairs of mirrored surfaces. Note that the discretization of boundary curves of mirrored surfaces, which actually precedes the surface discretization, is performed in a similar manner. In this case, however, the mirroring of appropriate pairs of curves (derived from the mirroring of opposite surfaces) is performed automatically by *T*3*d*.

A similar meshing strategy for PUCs was employed by Wentorf et al. [29]. In our framework, however, discretization is performed directly in the real space and the parametric space is used only for the mirroring of nodes. This concept avoids the demanding generation of anisotropic meshes in the parametric space, where distortion and stretching induced by the mapping may generally occur.

As mentioned in Section 1, the proposed numerical framework is based on a finite element scheme in which conventional (volumetric) elements are used to describe the response of the particles and the binder, while interfacial (cohesive) elements are introduced along the particle/matrix interface to model progressive interfacial failure during the debonding (or dewetting) process. Therefore, construction of cohesive elements is also necessary. This is enabled in the *T*3*d* framework by creating two identical curves in 2D and/or surfaces in 3D along which the cohesive elements are inserted. The same mirroring procedure as for the periodic sides of the unit cell is used to create two overlapping identical curve/surface meshes.

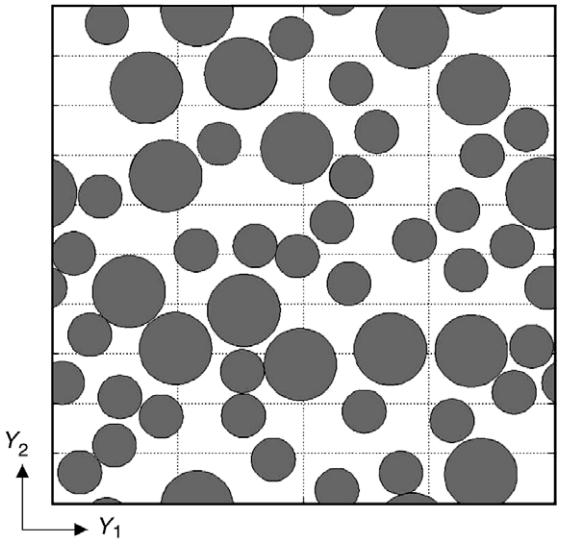

Fig. 4. 2D cell geometry of an idealized bimodal propellant PUC.

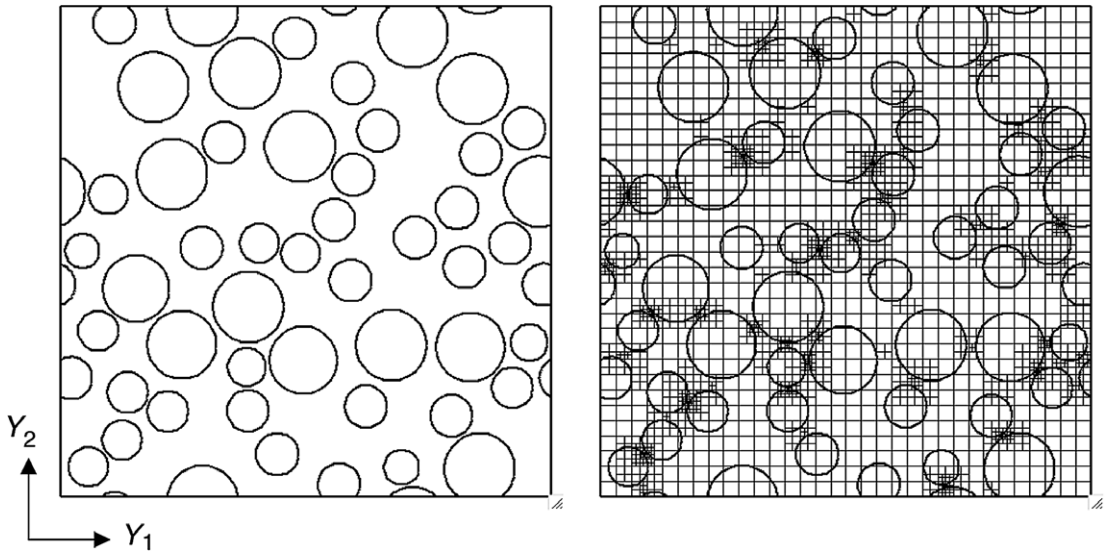

Fig. 5. Bezier curve representation (left) and refinement octree (right) of 2D PUC shown in Fig. 4.

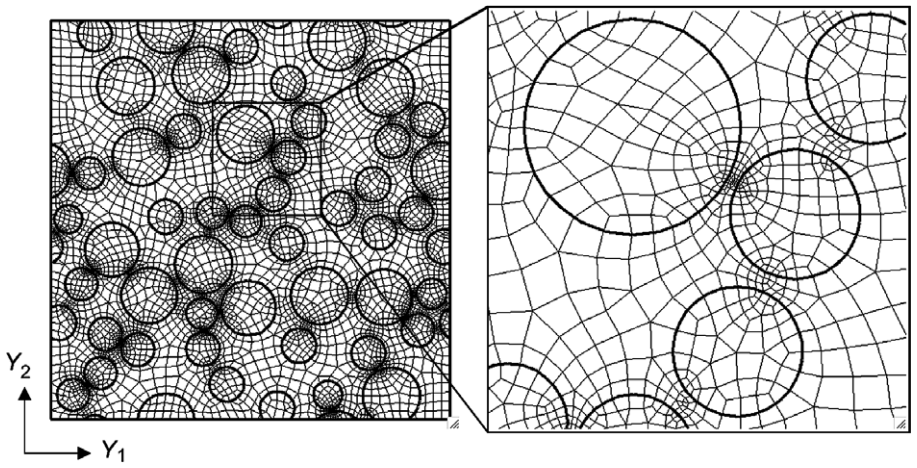

Fig. 6. High-quality mixed periodic mesh, composed of quadrilaterals and triangles.

Table 1
Finite element discretization for the 2D unit cell

	nn	*neQ*	*neT*	*nce*
Periodic mesh	7896	6146	184	1574

2.4. Examples – packing/pre-processing/meshing

We next demonstrate the packing/pre-processing/meshing procedures on an idealized propellant, with bimodal

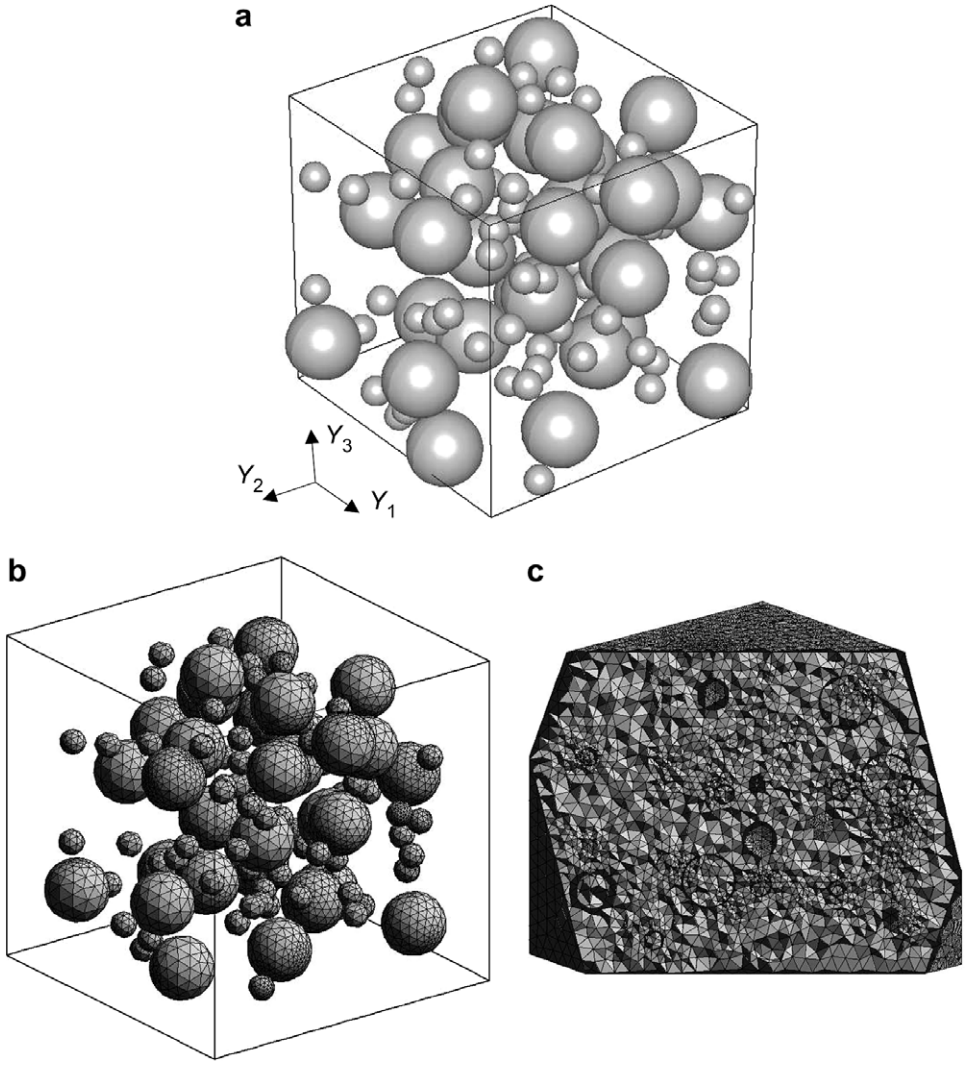

Fig. 7. An idealized bimodal propellant. 3D cell geometry and high-quality triangular (surface) and tetrahedral (volume) meshes.

particle distribution in a 2D periodic unit cell. Note that both packing and meshing can be executed without restrictions in 3D with features such as particle shrinking and non-uniform mesh size control fully operational. Moreover, the periodic boundary meshes for sides with cut particles would be identical to the 2D meshes presented here, since the only allowable geometrical entity after sphere cutting is a circle. A sphere in contact with the boundary box would be scaled down according to Eq. (2).

Fig. 4 shows an idealized 2D pack obtained from the packing algorithm (*Rocpack*). The pack is composed of a bimodal distribution of particle sizes and involves some contacting particles. After executing the pre-processing algorithm described above, we obtain a geometrical description based on rational Bezier curves/surfaces, where particles in contact with other particles and/or the reference box are modified according to Eq. (2) and a refinement parameter is set by Eq. (3). The 2D unit cell of dimensions 693×693 μm contains a bimodal pack, with diameters 100 μm (30% by volume of total particles) and 60 μm (70% by volume of total particles). The total particle volume fraction is 0.433. The original volume fraction of particles before particle shrinking was 0.451. The particle contraction has therefore led to a 3.9% change in the particle volume fraction. The error in converting the rational Bezier curves/surfaces to the finite element mesh in terms of volume fraction of particles is neglected due to high mesh refinement. Fig. 5 shows the resulting geometry and the refinement octree that governs the element size in the meshing procedure. The non-uniform mesh generated is displayed in Fig. 6. The characteristics of the 2D periodic mesh are listed in Table 1, where *nn* is the number of finite element nodes, *neQ* represents the number of volumetric quadrilateral elements, *neT* denotes the number of volumetric triangular elements, and *nce* is the number of cohesive elements.

An idealized 3D pack is obtained in a similar manner, as shown in Fig. 7. The unit cell consists of 100 reinforcing particles with a bimodal particle size distribution and the mesh contains 1,072,210 elements and 190,311 nodes.

3. Multiscale formulation of the damage response

Here, we describe the mathematical theory of homogenization and some aspects of its finite element implementation as used in this work to relate the complex damage processes taking place at the microscale to the homogenized macroscopic response of the reinforced elastomer. The formulation includes the cohesive modeling of particle–matrix debonding, but is limited to the small strain regime. The formulation presented hereafter is fully 3D, although the illustrative examples described in Section 4 are solved in a 2D (plane strain) setting.

3.1. Governing equations

Let us consider a periodic (Y-periodic) composite material with the microstructural period defined by the PUC created in Section 2 and denoted by Θ, as illustrated in Fig. 8. Next, consider $\boldsymbol{X} \in \mathbb{R}^3$ to be the position of a particle in the reference macroscopic configuration $\Omega \subset \mathbb{R}^3$ in the Cartesian co-ordinate system and $\boldsymbol{Y} = \boldsymbol{X}/\varsigma$ to be the microscopic position vector in $\Theta \subset \mathbb{R}^3$ in the Cartesian co-ordinate system. Hence, ς denotes a very small positive number that, roughly speaking, corresponds to the size of the microstructure. $\boldsymbol{X}$ is commonly referred to as the slow variable while $\boldsymbol{Y}$ is called the fast variable. The heterogeneity is enclosed by a cohesive surface S, and we orient the cohesive surface by a unit normal $\boldsymbol{N}$. For any macroscopically periodic function ϕ we have $\phi(\boldsymbol{X}, \boldsymbol{Y}) = \phi(\boldsymbol{X}, \boldsymbol{Y} + \boldsymbol{k}\widehat{\boldsymbol{Y}})$ in which vector $\widehat{\boldsymbol{Y}}$ is the basic period of the microstructure and $\boldsymbol{k}$ is a 3×3 diagonal matrix with integer components. Adopting the classical nomenclature, any locally Y-periodic function ϕ can be represented as

$$\phi^{\varsigma}(\boldsymbol{X}) \equiv \phi(\boldsymbol{X}, \boldsymbol{Y}(\boldsymbol{X})), \tag{4}$$

where the superscript "ς" denotes a Y-periodic function ϕ.

The corresponding boundary value problem at the microscale, including the cohesive description of the interface, is determined by the following set of governing equations:

$$\begin{aligned}
&\operatorname{div}(\boldsymbol{\sigma}^{\varsigma}) + \boldsymbol{f}^{\varsigma} = \boldsymbol{0} && \text{in} \quad \Omega^{\varsigma},\\
&\boldsymbol{\sigma}^{\varsigma} = \boldsymbol{L}\boldsymbol{\epsilon}^{\varsigma} && \text{in} \quad \Omega^{\varsigma},\\
&\boldsymbol{\epsilon}^{\varsigma} = \nabla^{s}\boldsymbol{u}^{\varsigma} && \text{in} \quad \Omega^{\varsigma},\\
&\boldsymbol{\sigma}^{\varsigma} \cdot \boldsymbol{N} = \underline{\boldsymbol{t}} && \text{on} \quad \Gamma_{\mathrm{t}},\\
&\boldsymbol{u}^{\varsigma} = \bar{\boldsymbol{u}} && \text{on} \quad \Gamma_{u},\\
&\lfloor \boldsymbol{\sigma}^{\varsigma} \cdot \boldsymbol{N} \rceil \equiv \lfloor \boldsymbol{t}^{\varsigma} \rceil = \boldsymbol{0} && \text{on} \quad S^{\varsigma},
\end{aligned} \tag{5}$$

where $\operatorname{div}(\bullet)$ is the divergence operator, ∇^s represents the symmetric gradient operator, and $\boldsymbol{\sigma}^{\varsigma}$ and $\boldsymbol{\epsilon}^{\varsigma}$ are stress and strain tensors, respectively. $\boldsymbol{L}(\boldsymbol{X},\boldsymbol{Y})$ denotes the spatially dependent symmetric material stiffness tensor, $\boldsymbol{f}(\boldsymbol{X},\boldsymbol{Y})$ denotes the body forces and $\underline{\boldsymbol{t}}(\boldsymbol{X})$ represents the prescribed macroscopic tractions on the boundary Γ_{t}. We also consider Dirichlet boundary conditions $\bar{\boldsymbol{u}}$ on Γ_u, such that $\Gamma = \Gamma_{\mathrm{t}} \cup \Gamma_u$. Moreover, the symbol $\lfloor \bullet \rceil$ denotes the jump of a quantity $\bullet$ across the cohesive surface. The cohesive

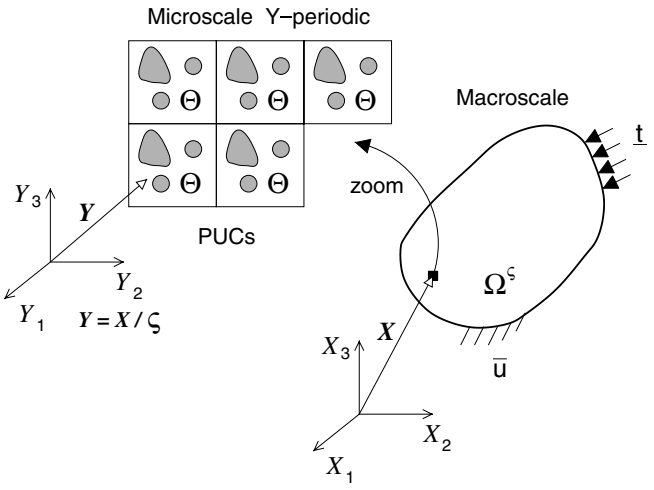

Fig. 8. Microscopic and macroscopic structures.

law used in this work to relate the cohesive traction acting along S^ς to the associated displacement jump vector $\lfloor \boldsymbol{u}^\varsigma \rceil$ is described later in this section.

3.2. Mathematical theory of homogenization

We start by approximating the displacement field $\boldsymbol{u}^\varsigma(\boldsymbol{X}) = \boldsymbol{u}(\boldsymbol{X}, \boldsymbol{Y})$ in terms of the two-scale asymptotic expansion on $\Omega \times \Theta$ as

$$\boldsymbol{u}(\boldsymbol{X}, \boldsymbol{Y}) \approx {}^0\boldsymbol{u}(\boldsymbol{X}, \boldsymbol{Y}) + \varsigma^1\boldsymbol{u}(\boldsymbol{X}, \boldsymbol{Y}) + \cdots, \tag{6}$$

where left superscripts "0,1,..." represent the asymptotic order. Employing the indirect macroscopic spatial derivatives, $\nabla^s_X = \nabla^s_X + \frac{1}{\varsigma}\nabla^s_Y$, the strain tensor reads

$$\boldsymbol{\epsilon}(\boldsymbol{X}, \boldsymbol{Y}) \approx \frac{1}{\varsigma}\nabla^s_Y {}^0\boldsymbol{u} + \varsigma^0\left(\nabla^s_X {}^0\boldsymbol{u} + \nabla^s_Y {}^1\boldsymbol{u}\right) + \cdots, \tag{7}$$

yielding strain tensors of various orders

$${}^{(-1)}\boldsymbol{\epsilon} = \nabla^s_Y {}^0\boldsymbol{u}, \qquad {}^0\boldsymbol{\epsilon} = \left(\nabla^s_X {}^0\boldsymbol{u} + \nabla^s_Y {}^1\boldsymbol{u}\right), \tag{8}$$

where ∇^s_X and ∇^s_Y, respectively, denote the symmetric part of the gradient with respect to $\boldsymbol{X}$ and $\boldsymbol{Y}$ coordinates. In this small strain linearly elastic setting, the stress and strain tensors for different orders of ς are related by the constitutive equations

$${}^{(-1)}\boldsymbol{\sigma} = \boldsymbol{L}^{(-1)}\boldsymbol{\epsilon}, \qquad {}^0\boldsymbol{\sigma} = \boldsymbol{L}^0\boldsymbol{\epsilon}, \tag{9}$$

and the resulting asymptotic expansion of the stress yields

$$\boldsymbol{\sigma}(\boldsymbol{X}, \boldsymbol{Y}) \approx \frac{1}{\varsigma}{}^{(-1)}\boldsymbol{\sigma} + {}^0\boldsymbol{\sigma} + \cdots \tag{10}$$

Applying standard variational methods, the principle of virtual work reads

$$\int_{\Omega^\varsigma} \boldsymbol{\sigma}^\varsigma : \nabla^s \delta\boldsymbol{u}\,\mathrm{d}\Omega + \int_{S^\varsigma} \boldsymbol{t}^\varsigma \cdot \lfloor \delta\boldsymbol{u} \rceil \mathrm{d}S - \int_{\Omega^\varsigma} \boldsymbol{f}^\varsigma \cdot \delta\boldsymbol{u}\,\mathrm{d}\Omega - \int_{\Gamma_t} \underline{\boldsymbol{t}} \cdot \delta\boldsymbol{u}\,\mathrm{d}A = 0 \tag{11}$$

for all admissible variations $\delta\boldsymbol{u}$ satisfying

$$\delta\boldsymbol{u} \in [H^1(\Omega^\varsigma)]^{\mathfrak{N}}, \qquad \delta\boldsymbol{u} = \boldsymbol{0} \quad \text{on } \Gamma_u, \tag{12}$$

with $\mathfrak{N}$ being the space dimension and H^1 representing the Sobolev space.

Introducing the asymptotic expansions (6) and (10) into (11), taking the limit when $\varsigma \to 0^+$ and making use of the indirect spatial derivatives, the principle of virtual work (11) holds in terms of the same powers of ς as

$$\begin{aligned}
&\mathcal{O}(\varsigma^{-2}) : \frac{1}{|\Theta|}\int_\Omega \int_\Theta {}^{(-1)}\boldsymbol{\sigma} : \nabla^s_Y \delta\boldsymbol{u}\,\mathrm{d}\Theta\,\mathrm{d}\Omega = 0,\\
&\mathcal{O}(\varsigma^{-1}) : \frac{1}{|\Theta|}\int_\Omega \int_\Theta \left[{}^{(-1)}\boldsymbol{\sigma} : \nabla^s_X \delta\boldsymbol{u} + {}^0\boldsymbol{\sigma} : \nabla^s_Y \delta\boldsymbol{u}\right]\mathrm{d}\Theta\,\mathrm{d}\Omega\\
&\qquad + \frac{1}{|\Theta|}\int_\Omega \int_S \boldsymbol{t} \cdot \lfloor \delta\boldsymbol{u} \rceil \mathrm{d}S\mathrm{d}\Omega = 0,\\
&\mathcal{O}(\varsigma^0) : \frac{1}{|\Theta|}\int_\Omega \int_\Theta {}^0\boldsymbol{\sigma} : \nabla^s_X \delta\boldsymbol{u}\,\mathrm{d}\Theta\,\mathrm{d}\Omega - \frac{1}{|\Theta|}\int_\Omega \int_\Theta \boldsymbol{f} \cdot \delta\boldsymbol{u}\,\mathrm{d}\Theta\,\mathrm{d}\Omega\\
&\qquad - \int_{\Gamma_t} \underline{\boldsymbol{t}} \cdot \delta\boldsymbol{u}\,\mathrm{d}A = 0
\end{aligned} \tag{13}$$

for $\forall \delta\boldsymbol{u} \in V_{\Omega\times\Theta}$, where

$$\begin{aligned}
V_{\Omega\times\Theta} &= \{\delta\boldsymbol{u}(\boldsymbol{X}, \boldsymbol{Y}) | \delta\boldsymbol{u}(\boldsymbol{X}, \boldsymbol{Y}) \in H^1(\Omega) \times L^2(\Omega; V^\bullet_\Theta),\\
&\qquad \delta\boldsymbol{u}(\cdot, \boldsymbol{Y}) \text{ is } Y\text{-periodic}, \delta\boldsymbol{u}|_{\Gamma_u} = \boldsymbol{0}\},\\
V_\Omega &= \{\delta\boldsymbol{u}(\boldsymbol{X}) | \delta\boldsymbol{u}(\boldsymbol{X}) \in H^1(\Omega),\ \delta\boldsymbol{u}|_{\Gamma_u} = \boldsymbol{0}\},\\
V_\Theta &= \{\delta\boldsymbol{u}(\boldsymbol{Y}) | \delta\boldsymbol{u}(\boldsymbol{Y}) \in H^1(\Theta),\ \delta\boldsymbol{u}(\boldsymbol{Y}) \text{ is } Y\text{-periodic}\},\\
V^\bullet_\Theta &= V_\Theta/\mathbb{R}.
\end{aligned} \tag{14}$$

Here, the $V^\bullet_\Theta$ is a quotient space, the uniqueness of ${}^1\boldsymbol{u}$ means that ${}^1\boldsymbol{u}(\boldsymbol{X}, \boldsymbol{Y})$ is uniquely defined up to the addition of an arbitrary function of $\boldsymbol{X}$. For more information on the space selection please see [30,31]. The following integration rules have been applied to integrate any *Y-periodic* function $\bullet$ [30,23]:

$$\begin{aligned}
&\lim_{\varsigma\to 0^+} \int_{\Omega^\varsigma} \bullet(\boldsymbol{X}/\varsigma)\,\mathrm{d}\Omega \to \frac{1}{|\Theta|}\int_\Omega \int_\Theta \bullet(\boldsymbol{Y})\,\mathrm{d}\Theta\,\mathrm{d}\Omega,\\
&\lim_{\varsigma\to 0^+} \varsigma \int_{S^\varsigma} \bullet(\boldsymbol{X}/\varsigma)\,\mathrm{d}S \to \frac{1}{|\Theta|}\int_\Omega \int_S \bullet(\boldsymbol{Y})\,\mathrm{d}S\,\mathrm{d}\Omega.
\end{aligned} \tag{15}$$

Let us first consider the $\mathcal{O}(\varsigma^{-2})$ Eq. (13_1) and choose $\delta\boldsymbol{u} = \delta\boldsymbol{u}(\boldsymbol{Y})$, i.e., $\delta\boldsymbol{u} \in V_\Theta$. Then, integrating by parts, applying the divergence theorem and noting that the terms on the opposite faces of the unit cell cancel due to the periodicity condition, one has

$$\nabla^s_Y \cdot {}^{(-1)}\boldsymbol{\sigma} = \boldsymbol{0} \quad \text{and} \quad {}^0\boldsymbol{u} = {}^0\boldsymbol{u}(\boldsymbol{X}) \ \Rightarrow\ {}^{(-1)}\boldsymbol{\epsilon} = {}^{(-1)}\boldsymbol{\sigma} = 0. \tag{16}$$

Using the results from Eq. (16), the $\mathcal{O}(\varsigma^{-1})$ equation with $\delta\boldsymbol{u} = \delta^1\boldsymbol{u} \in V_\Theta$ yields

$$\int_\Omega \left[\frac{1}{|\Theta|}\int_\Theta {}^0\boldsymbol{\sigma} : \nabla^s_Y \delta^1\boldsymbol{u}\,\mathrm{d}\Theta + \frac{1}{|\Theta|}\int_S \boldsymbol{t} \cdot \lfloor \delta^1\boldsymbol{u} \rceil \mathrm{d}S\right]\mathrm{d}\Omega = 0, \tag{17}$$

where

$$\begin{aligned}
&{}^1\boldsymbol{u} \text{ is } Y\text{-periodic on } \Gamma_\Theta \text{ and } \delta^1\boldsymbol{u} \in H^1(\Theta),\\
&\delta^1\boldsymbol{u} \text{ is } Y\text{-periodic on } \Gamma_\Theta.
\end{aligned} \tag{18}$$

In principle, Eq. (17) represents the weak form of the equilibrium on the microscale Θ for purely kinematic boundary conditions. Moreover, to satisfy the equilibrium with the assumed neighboring PUCs, the stress on the boundary Γ_Θ will also be periodic.

Finally, the $\mathcal{O}(\varsigma^0)$ equation with $\delta\boldsymbol{u} = \delta^0\boldsymbol{u} \in V_\Omega$ denotes the weak form of the equilibrium equation on the macroscale

$$\int_\Omega \underline{\boldsymbol{\sigma}} : \nabla\delta^0\boldsymbol{u}\,\mathrm{d}\Omega - \int_\Omega \underline{\boldsymbol{f}} \cdot \delta^0\boldsymbol{u}\,\mathrm{d}\Omega - \int_{\Gamma_t} \underline{\boldsymbol{t}} \cdot \delta^0\boldsymbol{u}\,\mathrm{d}A = 0, \tag{19}$$

where the macroscopic stress tensor and body force vector are given by

$$\underline{\boldsymbol{\sigma}} = \frac{1}{|\Theta|}\int_\Theta {}^0\boldsymbol{\sigma}\,\mathrm{d}\Theta, \quad \underline{\boldsymbol{f}} = \frac{1}{|\Theta|}\int_\Theta \boldsymbol{f}\,\mathrm{d}\Theta, \tag{20}$$

with

$$^0\boldsymbol{u} = \bar{\boldsymbol{u}} \text{ on } \Gamma_u \quad \text{and} \quad \delta^0\boldsymbol{u} \in H^1(\Omega), \quad \delta^0\boldsymbol{u} = \boldsymbol{0} \text{ on } \Gamma_u. \tag{21}$$

Note that to apply the boundary conditions properly, since the periodicity breaks down close to $\partial\Omega^\varsigma$, one would need to introduce special boundary layer terms as suggested in [31] and solve additional PDEs on a half space with exponentially decaying coefficients. Here, we assume that the boundary layer does not influence the solution and that prescribed displacements are a macroscopic quantity only.

With the aid of Eqs. (8), (9) and (20), the first term in Eq. (19) can be written as

$$\int_\Omega \underline{\boldsymbol{\sigma}} : \nabla\delta^0\boldsymbol{u}\,\mathrm{d}\Omega = \int_\Omega \left\{ \left[\frac{1}{|\Theta|} \int_\Theta \boldsymbol{L} \left(\underbrace{\nabla_X^{S\,0}\boldsymbol{u}}_{\underline{\boldsymbol{\epsilon}}} + \underbrace{\nabla_Y^{S\,1}\boldsymbol{u}}_{\tilde{\boldsymbol{\epsilon}}} \right) \mathrm{d}\Theta \right] : \nabla\delta^0\boldsymbol{u} \right\} \mathrm{d}\Omega, \tag{22}$$

where $\underline{\boldsymbol{\epsilon}}(\boldsymbol{X}) = \nabla_X^{S\,0}\boldsymbol{u}$ denotes the macroscopic strain tensor (recall that $^0\boldsymbol{u} = {}^0\boldsymbol{u}(\boldsymbol{X})$), and $\tilde{\boldsymbol{\epsilon}}(\boldsymbol{X},\boldsymbol{Y}) = \nabla_Y^{S\,1}\boldsymbol{u}$ represents the microscopic fluctuation strain. Using separation of variables and introducing the fourth-order mechanical damage tensor, $\mathscr{A}$, the asymptotic expansion of the strain (7) can be written in terms of the macroscopic strain $\underline{\boldsymbol{\epsilon}}$ as

$$\boldsymbol{\epsilon} = [\boldsymbol{I} + \mathscr{G}]\underline{\boldsymbol{\epsilon}} \quad \text{and} \quad \tilde{\boldsymbol{\epsilon}}(\boldsymbol{X},\boldsymbol{Y}) = \mathscr{G}(\boldsymbol{Y})\underline{\boldsymbol{\epsilon}}(\boldsymbol{X}), \tag{23}$$

where $\mathscr{A} = [\boldsymbol{I} + \mathscr{G}]$ and $\boldsymbol{I}$ denotes the fourth-order identity tensor, while $\mathscr{G}(\boldsymbol{Y})$ is the Y-periodic damage polarization function. Note that the mechanical damage tensor $\mathscr{A}$ contains both the elastic concentration function, which arises due to the material heterogeneity, and the damage transformation function, which originates due to the gradual debonding along the particle matrix interface and is related to the displacement jump introduced in Section 3.3. Separation of these effects is non-trivial and would require the introduction of a certain eigenstrain field. Therefore, we have combined both effects into one tensor, which is handily numerically computed.

Substituting (23) back into (22), we arrive at

$$\int_\Omega \underline{\boldsymbol{\sigma}} : \nabla\delta^0\boldsymbol{u}\,\mathrm{d}\Omega = \int_\Omega [\underline{\mathscr{L}}\,\underline{\boldsymbol{\epsilon}}] : \nabla\delta^0\boldsymbol{u}\,\mathrm{d}\Omega, \tag{24}$$

where the instantaneous macroscopic stiffness tensor is given by

$$\underline{\mathscr{L}} \equiv \frac{1}{|\Theta|} \int_\Theta \boldsymbol{L}\mathscr{A}\,\mathrm{d}\Theta, \tag{25}$$

and the macroscopic stress–strain law yields

$$\underline{\boldsymbol{\sigma}} = \underline{\mathscr{L}}\,\underline{\boldsymbol{\epsilon}}. \tag{26}$$

Note that the instantaneous macroscopic stiffness tensor is influenced by inhomogeneous material variations and the cohesive interface. Also, it can be proven that $\underline{\mathscr{L}}$ possesses the same minor and major symmetries as $\boldsymbol{L}$ [32].

3.3. Irreversible cohesive law

Cohesive models are popular in computational mechanics and have been extensively used in many different contexts [33–35]. The cohesive law adopted in this work to model the progressive failure of the particle–binder interface is the simple bilinear law used by Geubelle and Baylor [36], in which the normal and tangential components of the cohesive tractions, t_n and t_t, are related to the normal and tangential opening displacements, χ_n and χ_t, through

$$t_\mathrm{n} = \begin{cases} \frac{\sigma_\mathrm{c}}{\gamma_\mathrm{in}} \frac{\gamma}{1-\gamma} \frac{\chi_\mathrm{n}}{\chi_{\mathrm{n_c}}}, & \chi_\mathrm{n} \geqslant 0, \\ \frac{\tau_\mathrm{c}}{1-\gamma_\mathrm{in}} \frac{\chi_\mathrm{n}}{\chi_{\mathrm{n_c}}}, & \chi_\mathrm{n} < 0, \end{cases} \tag{27}$$

$$\boldsymbol{t}_\mathrm{t} = \frac{\tau_\mathrm{c}}{\gamma_\mathrm{in}} \frac{\gamma}{1-\gamma} \frac{\boldsymbol{\chi}_\mathrm{t}}{\chi_{\mathrm{t_c}}}, \tag{28}$$

where

$$\chi_\mathrm{n} = \lfloor {}^1\boldsymbol{u} \rceil \cdot \boldsymbol{N}, \qquad \boldsymbol{\chi}_\mathrm{t} = (\boldsymbol{I} - \boldsymbol{N}\otimes\boldsymbol{N})\lfloor {}^1\boldsymbol{u} \rceil. \tag{29}$$

Recall that $\lfloor {}^1\boldsymbol{u} \rceil$ denotes the jump of the fluctuating displacement across the cohesive surface and $\boldsymbol{N}$ represents the normal to the cohesive surface. The traction vector $\boldsymbol{t}$ introduced in Eq. (5) is, as expected, constructed as $\boldsymbol{t} = \boldsymbol{R}^\mathrm{T}\boldsymbol{t}_l$, where $\boldsymbol{t}_l = (t_{t1}, t_{t2}, t_\mathrm{n})^\mathrm{T}$ and $\boldsymbol{R}$ defines the orthogonal transformation from the global reference frame to the element specific (local) coordinate system. Standard isoparametric element procedure yields the required rotation matrix $\boldsymbol{R}$. The parameters σ_c and τ_c denote the tensile and shear interface strengths, respectively, while $\chi_{\mathrm{n_c}}$ and $\chi_{\mathrm{t_c}}$ represent the normal and tangential critical opening displacements. The normal and tangential directions are coupled through the damage parameter, γ, defined by

$$\gamma = \left\langle 1 - \sqrt{\left(\frac{\chi_\mathrm{n}}{\chi_{\mathrm{n_c}}}\right)^2 + \left(\frac{|\boldsymbol{\chi}_\mathrm{t}|}{\chi_{\mathrm{t_c}}}\right)^2} \right\rangle \quad \forall \chi_\mathrm{n} \geqslant 0, \tag{30}$$

with $\langle\bullet\rangle$ denoting McAuley brackets. As apparent in Eqs. (27) and (28), a decreasing value of γ leads to an increasingly compliant cohesive interface. γ is initially set to a value γ_in, taken to be 0.98. Once $\gamma < \gamma_\mathrm{in}$, the traction carried by the interface begins to reduce and the interface is considered to be locally damaged. The interface continues to degrade with decreasing γ and increasing separation of the interface until $\gamma = 0$. At this point, the local interface is considered to be completely failed. In the case of compression ($\chi_\mathrm{n} < 0$), no damage is accumulated. The cohesive model described above is irreversible; γ is only allowed to decrease monotonically so that, even if the interface is unloaded, it retains the current state of damage and unloading is towards the origin. The bilinear law is represented graphically in Fig. 9.

3.4. Numerical implementation

Euler–Lagrange equations on the microscale $\mathscr{O}(\varsigma^{-1})$ (13_2) and on the macroscale, $\mathscr{O}(\varsigma^0)$ (13_3), are solved with a conventional finite element scheme. A $\overline{\boldsymbol{B}}$ procedure is

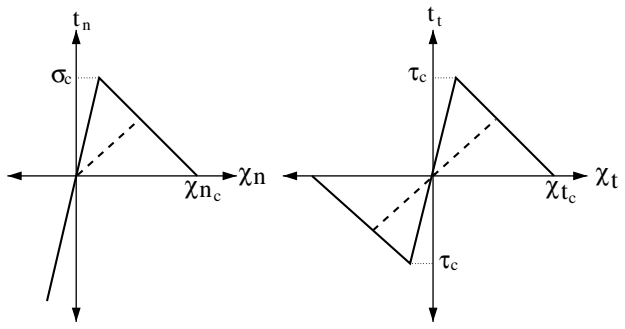

Fig. 9. Bilinear cohesive law for normal separation (left) and tangential failure (right). The dashed line indicates an unloading path prior to complete failure. The normal and shear failures are coupled through the damage parameter γ, defined in Eq. (30).

used to eliminate pressure oscillations and create a stable 2D finite element framework for nearly incompressible materials. Cohesive elements are inserted at the particle–matrix interfaces and a three-point integration rule is used, with the local damage parameter γ stored as a state variable at each integration point. The choice of $\gamma_{in} < 1$ introduces a small amount of compliance into the undamaged cohesive interface, eliminating the numerical instabilities associated with rigid elements.

The numerical implementation uses a semi-implicit solution procedure with adaptive load stepping to ensure efficiency of computational effort. When no damage is accumulated, the model is linear, allowing for larger load steps. As damage increases, however, smaller load steps are required in order to capture accurately the physics of the failure process, suggesting the introduction of an adaptive load-stepping scheme. The maximum increment of damage accumulated at any integration point in a load step is used as an error indicator to determine whether the load-step size needs to be reduced or increased. If the accumulated damage γ is greater than a certain threshold, γ_{max}, the load-step size is reduced and the current load step is restarted. This is similar to a predictor–corrector method. If the damage accumulated is less than γ_{min}, the load-step size for future load steps is increased. Typically, the value used for γ_{min} is half that for γ_{max}, which is in the range of 0.01–0.001.

4. Examples

To illustrate the proposed multiscale numerical framework, we analyze the damage evolution in the model 2D particulate composite system shown earlier. To analyze more representative unit cells, high-performance parallel computing is necessary due to the size and complexity of the finite element model. Finite element meshes are created as described in Section 2. All constituents are assumed to be isotropic linearly elastic solids. The elastic material characteristics (stiffness E and Poisson's ratio ν) of the particles and of the homogenized blend (consisting of the binder and small particles) are listed in Table 2. Note the very high stiffness mismatch between the particle and the blend and the near incompressibility of the blend, as quantified by the Poisson's ratio approaching 1/2. The interface properties, given in Table 3, have been chosen to ensure that failure occurs within the limit of small strains. The stresses in the surrounding material are influenced by the strength of the cohesive interface. Therefore, low macroscopic stresses are observed in the results presented below.

Table 2
Material properties

Constituent	E (MPa)	ν
Particles	32,450	0.1433
Binder	7.39	0.4991

Instead of solving the macroscopic boundary value problem explicitly, $\mathcal{O}(\varsigma^0)$ Eq. (13_2), we impose hereafter a predefined deformation path of a macroscale material point as in the microhistory recovery procedure proposed by Fish et al. [37]. Three loading cases are considered here, characterized by the following macroscopic strains, $\underline{\boldsymbol{\epsilon}}$:

$$\underline{\boldsymbol{\epsilon}}^{A} = \begin{bmatrix} 0.01 & 0.00 \\ 0.00 & -0.01 \end{bmatrix}, \quad \underline{\boldsymbol{\epsilon}}^{B} = \begin{bmatrix} 0.01000 & 0.00000 \\ 0.00000 & -0.00982 \end{bmatrix}, \quad \underline{\boldsymbol{\epsilon}}^{C} = \begin{bmatrix} 0.00 & 0.02 \\ 0.02 & 0.00 \end{bmatrix}. \tag{31}$$

The third row and column of the macroscopic strain tensors are not shown as these are zero under plane strain conditions. Cases A and C are volume preserving macroscopic strains and are equivalent in terms of principal stresses. Case B is a quasi-uniaxial stress, which is achieved by imposing a strain which is a slight deviation from load case A in order to study the dilatational stress component (pressure $\underline{p} = 1/3\,\mathrm{tr}(\underline{\boldsymbol{\sigma}})$) resulting from the attempt to force a nearly incompressible cell to deform in a non-volume preserving manner.

4.1. Load cases A and B

Fig. 10 shows the macroscopic stress–strain curve (left axis) and evolution of interfacial damage (right axis) for the volume preserving tension case (load case A). The solid line denotes macroscopic stress in the direction of applied tension, $\underline{\sigma}_{11}$. The dash-dotted curve corresponds to the evolution of cohesive interface elements which have begun to experience damage, defined as elements for which $\gamma < \gamma_{in}$.

Table 3
Cohesive interface properties

Direction	Interface strength (MPa)	Critical opening displacement (μm)
Normal	$\sigma_c = 0.05$	$\chi_{n_c} = 0.75$
Tangential	$\tau_c = 0.05$	$\chi_{t_c} = 0.75$

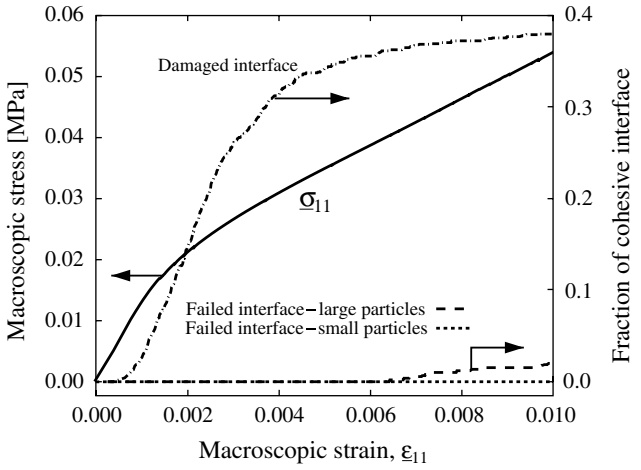

Fig. 10. Load case A – Macroscopic stress–strain and damage curves. The interface is considered to be damaged when $\gamma < \gamma_{in}$ and failed when $\gamma = 0$.

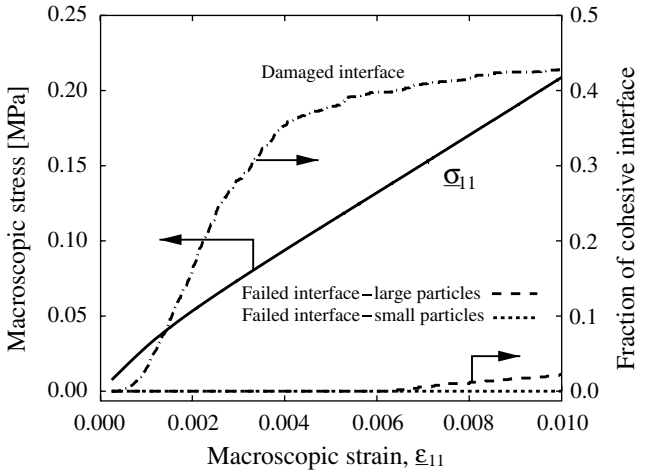

Fig. 11. Load case B – Macroscopic stress–strain and damage curves.

The length of damaged cohesive interface is divided by the total interface length to obtain the damaged fraction. This represents the portion of the interface which is in the cohesive zone (softening part of the traction–separation curve). The dashed and dotted curves indicate the fraction of fully failed cohesive elements on the boundaries of large and small particles, respectively, where fully failed elements are those for which $\gamma = 0$.

It is clear that the initial deviation from linearity of the material response is a result of the onset of damage of the cohesive elements. This early damage is fairly evenly distributed throughout the microstructure, with no significant difference between interfaces associated with large and small particles. The locations at which damage nucleates depend on local stress concentrations, but not on the size of the particles. For this reason, only a single curve is plotted, representing the damage fraction over all cohesive interfaces. Damage of the cohesive interface saturates at the point at which complete failure begins to be observed.

In contrast to damage nucleation, the failure of the interfaces shows a marked size effect. As often observed experimentally, most of the failure occurs on large particle interfaces, and very little on interfaces associated with small particles. The failure process is discrete, with only a few particles failing at a time. Once failure initiates on a particle, the increased compliance of the failing interface causes load redistribution such that failure does not, in many cases, initiate elsewhere until it is complete for that particle.

The imposed strain for load case B, $\underline{\epsilon}^{B}$, was chosen by trial and error such that $\underline{\sigma}_{22} \approx 0$ (uniaxial tension loading case). The damage and failure responses, shown in Fig. 11, are very similar to those for load case A. However, the macroscopic stress–strain response is markedly different. Due to the quasi-incompressibility of the binder and the quasi-rigidity of the embedded particles, there is a significant change in the state of stress for load case B, where the imposed strain is not volume preserving, resulting in a rapid increase in the dilatational component of the stress (pressure). The large difference in macroscopic response between load cases A and B is clearly seen in Fig. 12. For both cases, although 40% of the interface has begun to degrade, the macroscopic stress continues to grow monotonically. One might assume that stress softening would dominate the behavior once such a large percentage of the interface has degraded. This weak non-linearity is associated in part with the constrained loading cases considered. The compression of the nearly incompressible and compliant blend against the hard particles also serves to prevent the propagation of the debonding cracks.

If we exclude dilatational stress from our analysis by considering a deviatoric measure of the stress field, such as the von Mises stress, we find that load cases A and B are nearly identical. The von Mises stress distribution for load case A is shown on the deformed mesh in Fig. 13.

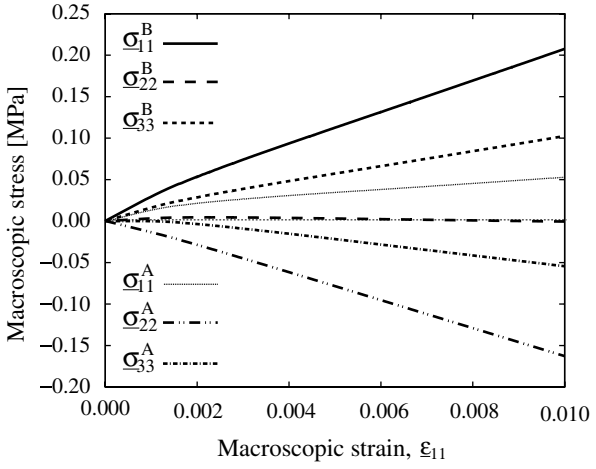

Fig. 12. Macroscopic stress–strain curves — Comparison between volume preserving (case A) and quasi-uniaxial loading (case B). The large difference in stress response with only a small difference in applied macroscopic strain is explained by the increased dilatational stress for load case B, which is not volume preserving.

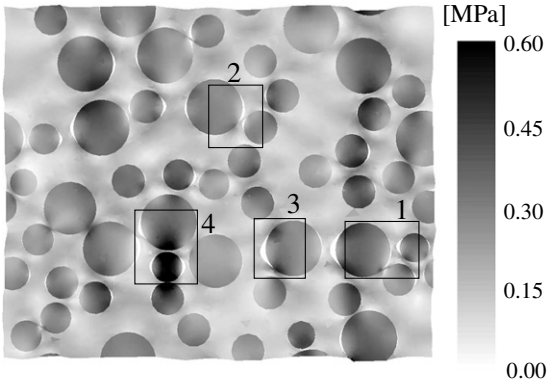

Fig. 13. Load case A – von Mises stress distribution plotted on the deformed configuration with displacements magnified 10 times. The numbers refer to comments in the text.

The deformation is magnified 10 times, so that the opening of cohesive interfaces is easily visible. Void opening is aligned with applied load, i.e., on the left and right edges of the particles (box 1), however, in box 2, we note that a stress concentration due to particle proximity causes the voids to open on a slightly different face. Stress concentrations at the crack tips can be seen, in box 3 particularly. Note the heterogeneous stress distribution in the matrix material and the periodicity of the boundaries.

As expected from the macroscopic response, failure occurs predominantly on large particles. Small particles fail primarily when they are in an area of local stress concentration, e.g., close to another particle. Examples of such failures can be found in Fig. 13, with particle pairs failing in tension (box 1) or in shear (box 4).

If we compare results from the same load case applied to different unit cells (Fig. 14), we see a minor deviation in the macroscopic stress. Since the emphasis of this paper is not to investigate the size of the representative volume element, we make no claim on representativeness of this comparison. One would need to compute the bounds on the solution with respect to the cell size to determine the representativeness of these results. Unit cells (a) and (b) are identical in terms of geometric statistics, but differ in the arrangement of particles within the domain. In particular, cell (b) is obtained by rotating cell (a) by 90°, but the finite element meshes are identical for both cells to eliminate the numerical errors in the comparison. The initial (undamaged) stiffness is in agreement, but after onset of damage, cell (a) is seen to be more compliant than cell (b). The reason for this difference might be explained by comparing the evolution of damage for the two cases (Fig. 15). The curves shown on the right two figures denote the percentile of degraded interface for a particular value of γ defined by (30). No curve is plotted for $\gamma = 0.98$, as the fraction of cohesive elements with $\gamma \leqslant 0.98$ is identically 1 at all times. The $\gamma = 0.95$ curve represents the fraction of the cohesive interface which has experienced any damage, equivalent to the dash-dotted line in Fig. 10. The $\gamma = 0.0$ curve represents the fraction of the cohesive interface which has completely failed, equivalent to the average of the dashed and dotted curves in Fig. 10. The spacing between contours indicates how rapidly damage progresses. It is clear that damaged elements proceed to failure more suddenly in cell (a) than in cell (b). A higher fraction of the cohesive interface experiences the onset of damage in cell (b) than in cell (a), but a lower fraction of the cohesive interface experiences complete failure. This lower fraction of failed interface suggest increased stiffness of the macroscopic stress–strain response for cell (b). Considering the deformed shapes, we can see that more of the damaged interfaces in cell (a) have opened up to form voids than those in cell (b). Since the microscopic damage processes for both cells are markedly different, but macroscopic stress–strain curves disagree only slightly, one might assume that the cells are representative. Although, a more detailed investigation is needed to assess the representativeness of these cells.

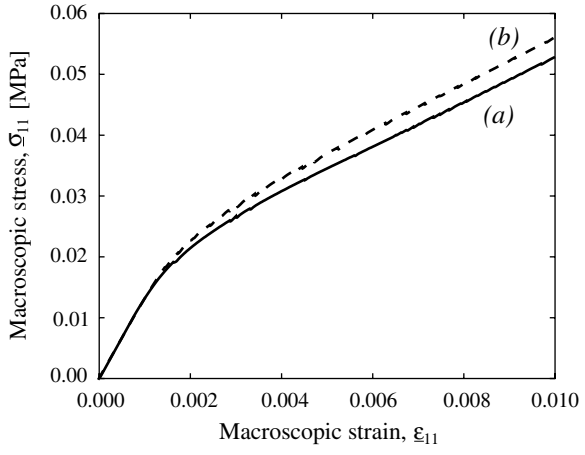

Fig. 14. Load case A – Macroscopic stress–strain curves obtained for two different periodic unit cells.

4.2. Load case C

The macroscopic response for load case C, a volume-preserving imposed shear state of macroscopic strain, is shown in Fig. 16, with the corresponding von Mises stress distribution presented in Fig. 17. Again, the periodicity of the computed fields is evident. The fluctuating displacements can also be distinguished by observing the heterogeneity of the boundary deformations. The von Mises stress distribution is heterogeneous, showing the effects of multiple stress concentrations. Void opening is aligned with the principal tensile stress direction of 45°.

Particle pairs separate in opening (box 1) or in shearing (boxes 2 and 3). In box 1, interfacial failure for the particle pair initiates in alignment with the highest stress concentration. Failure is often associated with the rotation of the particle, resisted by the surrounding matrix. This tendency to rotation is apparent for boundary particles 4 and 5. For this reason, voids do not open as much as for load case A.

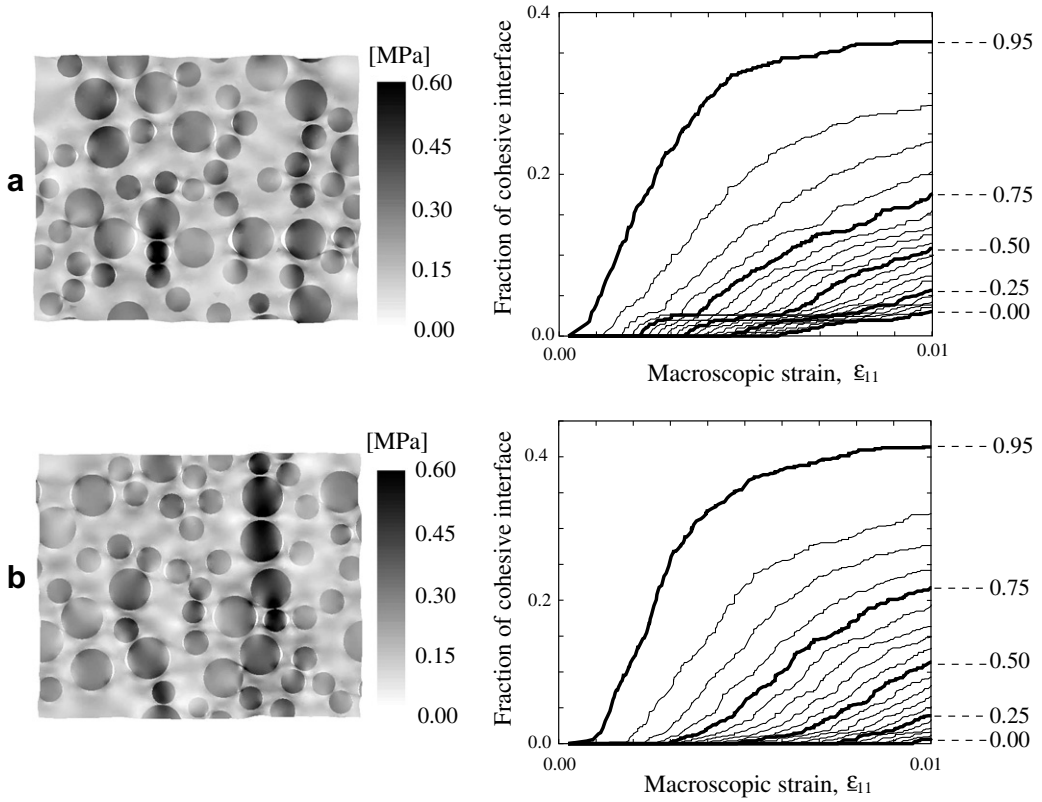

Fig. 15. Load case A – Details of the microscopic damage for the two periodic unit cells whose macroscopic response is presented in Fig. 14. von Mises stress distribution for $\epsilon_{11} = 0.01$ (left); Damage evolution curves for 20 values of the damage parameter γ (right).

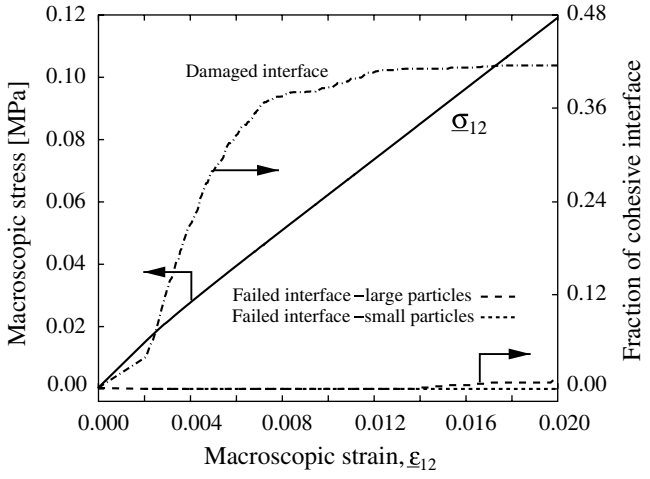

Fig. 16. Load case C – Macroscopic stress–strain and damage curves.

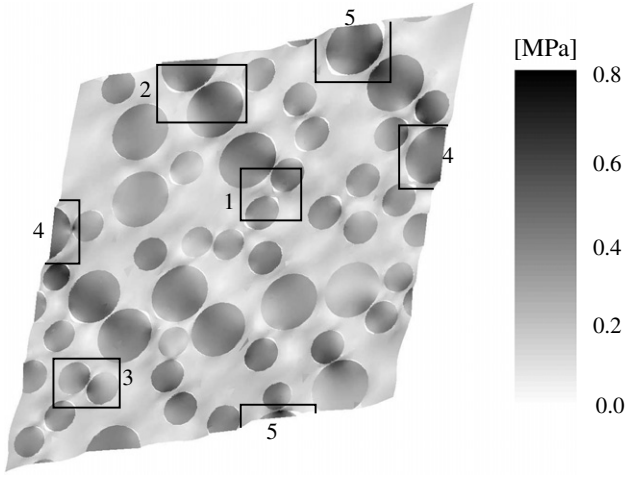

Fig. 17. Load case C – von Mises stress distribution plotted on a deformed mesh with displacements magnified 10 times. Numbers 1–5 refer to features discussed in the text.

It was noted that volume preserving tension and shear are identical in terms of principal stresses. This is clear if we compare the von Mises stress fields for load cases A and C. Rotating Fig. 17 so that the principal stresses are aligned with those in Fig. 13, we see bands of increased stress running along the major tension axis, and maximum opening on the transverse edges of the particles.

The similarity between load cases A and C is further evident through comparison between Figs. 16 and 10. The damage fraction rises early, and then levels off to form a plateau, a significant feature in both curves, indicating that damage propagation stops due to the transverse compressive effect. At this point, interfaces fail completely, as evident in the failure fraction curves. This late opening of voids, however, may be due to the choice of cohesive interface properties, and in particular, the choice of high critical

opening displacements. In order to simulate a failure process more representative of actual solid propellant behavior, we would need to use a non-linear kinematic formulation. The monotonically increasing stress–strain curve is, once again, associated with the near incompressibility of the blend.

5. Conclusions

A fully automated mathematical/numerical framework for multiscale modeling of heterogeneous propellants from particle packing to failure has been presented. The microscale description is based on a periodic unit cell consisting of particles dispersed in a blend and incorporates the local non-homogeneous stress and deformation fields present in the unit cell during the failure of the particle/matrix interfaces. A packing algorithm, treating the embedded particles as spheres or discs, is used to generate packs which match the size distribution and volume fraction of actual propellants. Moreover, a sophisticated pre-processing tool has been developed to generate a geometric model based on Bezier curves and/or surfaces. This geometric model is then used in a general meshing tool, *T*3*d*, to create high-quality periodic meshes. Since the identical meshing of the periodic entities using the advancing front technique is not usually viable, a different approach based on mirroring has been adopted. Next, the mathematical theory of homogenization based on the asymptotic expansion of the displacement, strain and stress fields has been derived and used in modeling debonding (or dewetting) damage evolution in reinforced elastomers.

Various examples involving 2D unit cells and macroscopic deformation histories of an idealized solid propellant have been considered to study the link between the failure process taking place at the particle size scale and its effect on the macroscopic stress–strain curves and the evolution of void volume. The emphasis of this work has been to develop a damage analysis tool at multiple scales from particle packing to failure. Further research will involve the inclusion of large deformations, a more complex, rate-dependent description of the binder and a matrix tearing model needed to capture the initiation and propagation of cracks in the solid propellant during void coalescence. Moreover, the size of the representative volume element in the presence of damage needs to be investigated.

Acknowledgements

The work of K. Matouš, H.M. Inglis, X. Gu, T.L. Jackson and P.H. Geubelle was supported by the Center for Simulation of Advanced Rockets (CSAR) under contract number B341494 by the US Department of Energy as a part of its Advanced Simulation and Computing program (ASC). K. Matouš and P.H. Geubelle also acknowledge support from ATK/Thiokol, with J. Thompson and Dr. I.L. Davis as a program monitors. The work of Dr. Rypl was supported by the Grant Agency of the Czech Republic under contract number GAČR 103/05/2315.

References

[1] Ha K, Schapery RA. A three-dimensional viscoelastic constitutive model for particulate composites with growing damage and its experimental validation. Int J Solids Struct 1998;26(27):3497–517.
[2] Simo JC. On a fully three-dimensional finite-strain viscoelastic damage model: formulation and computational aspects. Comp Meth Appl Mech Engng 1987;60:153–73.
[3] Mullins L. Softening of rubber by deformation. Rubber Chem. Tech. 1969;42:339–61.
[4] Farris RJ. The character of the stress–strain function for highly filled elastomers. Trans Soc Rheol 1968;12:303–14.
[5] Christensen RN, Lo KH. Solutions for effective properties of composite materials. J Mech Phys Solids 1979;27:315–30.
[6] Hutchinson JW, Jensen HM. Models of fiber debonding and pullout in brittle composites with friction. Mech Mater 1990;9:335–442.
[7] Hashin Z. The spherical inclusion with imperfect interface. ASME J Appl Mech 1991;58:444–9.
[8] Matouš K. Damage evolution in particulate composite materials. Int J Solids Struct 2003;40:1489–503.
[9] Krajcinovic D. Damage mechanics. Amsterdam: Elsevier Science; 1996.
[10] Chaboche JL, Kruch S, Maire JF, Poittier T. Towards a micromechanics based inelastic and damage modeling of composites. Int J Plasticity 2001;17:411–39.
[11] Zhong AX, Knauss WG. Analysis of interfacial failure in particle-filled elastomers. J Engng Mater Technol 1997;119:198–204.
[12] Zhong AX, Knauss WG. Effects of particle interaction and size variation on damage evolution in filled elastomers. Mech Compos Mater Struct 2000;7:35–53.
[13] Michel JC, Moulinec H, Suquet P. Effective properties of composite materials with periodic microstructure: a computational approach. Comp Meth Appl Mech Engng 1999;172:109–43.
[14] Segurado J, Llorca J. A numerical approximation to the elastic properties of sphere-reinforced composites. J Mech Phys Solids 2002;50:2107–21.
[15] Llorca J, Segurado J. Three-dimensional multiparticle cell simulations of deformation and damage in sphere-reinforced composites. Mater Sci Engng A 2004;365:67–274.
[16] Knott GM, Jackson TL, Buckmaster J. The random packing of heterogeneous propellants. AIAA J 2001;39(4):678–86.
[17] Kochevets S, Buckmaster J, Jackson TL, Hegab A. Random propellant packs and the flames they support. AIAA J Propul Power 2001;17(4):883–91.
[18] Rypl D. Sequential and parallel generation of unstructured 3D meshes. PhD thesis. CTU Reports, vol. 3, no. 2. Prague: Czech Technical University; 1998. *T*3*d* page. Available from: http://mech.fsv.cvut.cz/~dr/t3d.html.
[19] Rypl D, Bittnar Z. Hybrid method for generation of quadrilateral meshes. Engng Mech 2002;9(1/2):49–64.
[20] Hughes TJR. The finite element method, linear static and dynamic finite element analysis. New Jersey: Prentice-Hall, Inc. A Division of Simon & Schuster; 1987.
[21] Matouš K, Geubelle PH. Multiscale modeling of particle debonding in reinforced elastomers subjected to finite deformations. Int J Numer Meth Engng 2006;65:190–223.
[22] Fish J, Yu Q. Multiscale damage modeling for composite materials: theory and computational framework. Int J Numer Meth Engng 2001;52(1–2):161–92.
[23] Guedes JM, Kikuchi N. Preprocessing and postprocessing for materials based on the homogenization method with adaptive finite element methods. Comp Meth Appl Mech Engng 1990;83(1–2):143–98.

[24] Wang X, Buckmaster J, Jackson TL. Burning of ammonium-perchlorate ellipses and spheroids in fuel binder. AIAA J Propul Power 2006;22(4):764–8.
[25] McGeary RK. Mechanical packing of spherical particles. J Am Ceram Soc 1961;44(10):513–22.
[26] Miller RR. Effects of particle size on reduced smoke propellant ballistics. Paper No. 82-1096. AIAA; 1982.
[27] Zeman J, Šejnoha M. Numerical evaluation of effective elastic properties of graphite fiber tow impregnated by polymer matrix. J Mech Phys Solids 2001;49:69–90.
[28] Bittnar Z, Rypl D. Direct triangulation of 3D surfaces using advancing front technique. In: Proceedings of the second ECCOMAS conference on numerical methods in engineering. Paris, France: Wiley; 1996. p. 86–90.
[29] Wentorf R, Collar R, Shephard MS, Fish J. Automated modeling for complex woven mesostructures. Comput Meth Appl Mech Engng 1999;172(1–4):273–91.
[30] Bensoussan A, Lions JL, Papanicolaou G. Asymptotic analysis for periodic structures. New York: North-Holland; 1978.
[31] Lions JL. Some methods in the mathematical analysis of systems and their control. New York: Gordon and Breach; 1981.
[32] Duvaut G. Homogeneization et materiaux composites. In: Ciarlet PG, Rouseau M, editors. Trends and applications of pure mathematics to mechanics. Lecture notes in physics, vol. 195. Berlin: Springer; 1984.
[33] Ortiz M, Pandolfi A. Finite-deformation irreversible cohesive element for three-dimensional. crack-propagation analysis. Int J Numer Meth Engng 1999;44:1267–82.
[34] Roy YA, Dodds RH. Simulation of ductile crack growth in thin aluminum panels using 3-D surface cohesive elements. Int J Fracture 2001;110:21–45.
[35] Xu XP, Needleman A. A numerical study of dynamic crack growth in brittle solids. Int J Solids Struct 1994;84:769–88.
[36] Geubelle PH, Baylor JS. Impact-induced delamination of composites: a 2D simulation. Composites B 1998;29:589–602.
[37] Fish J, Shek K, Pandheeradi M, Shephard MS. Computational plasticity for composite structures based on mathematical homogenization: theory and practice. Comp Meth Appl Mech Engng 1997;148:53–73.